optica

Resonantly enhanced nonreciprocal silicon Brillouin amplifier: supplementary material

NILS T. OTTERSTROM[1,4], ERIC A. KITTLAUS[1], SHAI GERTLER[1], RYAN O. BEHUNIN[2], ANTHONY L. LENTINE[3], AND PETER T. RAKICH[1,5]

[1]Department of Applied Physics, Yale University, New Haven, Connecticut 06520 USA
[2]Department of Physics and Astronomy, Northern Arizona University, Flagstaff, Arizona 86001 USA
[3]Applied Photonic Microsystems, Sandia National Laboratories, Albuquerque, New Mexico 87185, USA
[4]e-mail: nils.otterstrom@yale.edu
[5]e-mail: peter.rakich@yale.edu

Published 27 August 2019

This document provides supplementary information to "Resonantly enhanced nonreciprocal silicon Brillouin amplifier," https://doi.org/10.1364/OPTICA.6.001117.

1. DYNAMICS OF RESONANTLY ENHANCED BRILLOUIN AMPLIFIER

A. Mean-field analysis

In this section, we describe a simple mean-field treatment of the amplifier dynamics that is sufficient to capture the salient behavior of the resonantly enhanced intermodal Brillouin process. Combining mean-field analysis of the full spatio-temporal dynamics of a resonant Brillouin system (see Supplementary Materials of Ref. [1]) with standard coupled-mode theory [2], we can express the equations of motion as

$$\begin{aligned}
\dot{a}_{\mathrm{s}}(t) &= -i\omega_1^n a_{\mathrm{s}}(t) - \frac{\gamma_{\mathrm{tot},1}}{2} a_{\mathrm{s}}(t) - ig^* a_{\mathrm{p}}(t) b^\dagger(t) + \sqrt{\gamma_{\mathrm{A},1}} S^{\mathrm{in}}(t) + \sqrt{\gamma_{\mathrm{A},1}} S_{\mathrm{A}}^{\mathrm{N}}(t) + \sqrt{\gamma_{\mathrm{B},1}} S_{\mathrm{B}}^{\mathrm{N}}(t) + \sqrt{\gamma_{\mathrm{R},1}} S_{\mathrm{R}}^{\mathrm{N}}(t) \\
\dot{b}(t) &= -i\Omega_{\mathrm{B}} b(t) - \frac{\Gamma}{2} b(t) - ig^* a_{\mathrm{p}}(t) a_{\mathrm{s}}^\dagger(t) + \eta(t) \\
\dot{a}_{\mathrm{p}}(t) &= -i\omega_2^m a_{\mathrm{p}}(t) - \frac{\gamma_{\mathrm{tot},2}}{2} a_{\mathrm{p}}(t) - iga_{\mathrm{s}}(t) b(t) + \sqrt{\gamma_{\mathrm{A},2}} S_{\mathrm{p}}^{\mathrm{in}}(t) + \sqrt{\gamma_{\mathrm{tot},2}} S_{\mathrm{tot},2}^{\mathrm{N}}(t).
\end{aligned} \tag{1}$$

Here, $a_{\mathrm{s}}(t)$, $b(t)$, and $a_{\mathrm{p}}(t)$ are the coupled-mode amplitudes for the signal, phonon, and pump fields, respectively, with units of $[\sqrt{\mathrm{number}}]$; $\{\omega_1^n\}$ and $\{\omega_2^m\}$ are the resonance frequencies of the cavity modes produced by the symmetric and antisymmetric waveguide modes, respectively; $S^{\mathrm{in}}(t)$ and $S_{\mathrm{p}}^{\mathrm{in}}(t)$ represent the input signal-wave and pump-wave fields (with units $[\sqrt{\mathrm{number} \times \mathrm{Hz}}]$); g is the acousto-optic coupling; $\eta(t)$ is the mechanical stochastic driving term that is consistent with the fluctuation-dissipation theorem, with a two-time correlation function of $\langle \eta(t')\eta^\dagger(t)\rangle = \Gamma(n_{\mathrm{th}}+1)\delta(t-t')$, where n_{th} is the thermal occupation of the phonon field;

$S^{\mathrm{N}}_{(\mathrm{A,B,R})}(t)$ represent the vacuum fluctuations associated with the optical losses produced by (A) coupler A, (B) coupler B, and (R) the intrinsic loss of the of the racetrack resonator, each with a two-time correlation function given by $\langle S^{\mathrm{N}}_{(\mathrm{A,B,R})}(t')S^{\mathrm{N\dagger}}_{(\mathrm{A,B,R})}(t)\rangle = \delta(t-t')$; $S^{\mathrm{N}}_{\mathrm{tot},2}(t)$ represents the vacuum fluctuations associated with the total loss experienced by an antisymmetric optical spatial mode; $\gamma_{\mathrm{tot},(1,2)}$ is the total loss rate for the symmetric and antisymmetric spatial modes (defined by $\gamma_{\mathrm{tot},(1,2)} \equiv \gamma_{\mathrm{A},(1,2)} + \gamma_{\mathrm{B},(1,2)} + \alpha_{(1,2)} v_{\mathrm{g},(1,2)}$); $\gamma_{(\mathrm{A,B}),(1,2)}$ are the dissipation rates for the symmetric and antisymmetric spatial modes due to couplers A and B ($\gamma_{(A,B),(1,2)} \equiv -(2v_{\mathrm{g},(1,2)}/L)\ln(1-\mu^2_{(\mathrm{A,B}),(1,2)})^{1/2}$) while $\gamma_{\mathrm{R},1}$ represents the internal losses of the racetrack resonator for the symmetric mode ($\gamma_{\mathrm{R},1} = \alpha_1 v_{\mathrm{g},1}$); $v_{\mathrm{g},(1,2)}$ is the group velocity of the symmetric and antisymmetric optical spatial modes; L is the length of the racetrack resonator; $\alpha_{(1,2)}$ is the linear propagation loss of the symmetric and antisymmetric spatial mode; Γ is the dissipation rate for the acoustic field.

Using the rotating-wave approximation, we center each field around DC, yielding

$$\begin{aligned}
\dot{\bar{a}}_{\mathrm{s}}(t) &= i(\omega_{\mathrm{s}} - \omega_1^n)\bar{a}_{\mathrm{s}}(t) - \frac{\gamma_{\mathrm{tot},1}}{2}\bar{a}_{\mathrm{s}}(t) - ig^*\bar{a}_{\mathrm{p}}(t)\bar{b}^{\dagger}(t) + \sqrt{\gamma_{\mathrm{A},1}}\bar{S}^{\mathrm{in}}(t) + \sqrt{\gamma_{\mathrm{A},1}}\bar{S}^{\mathrm{N}}_{\mathrm{A}}(t) + \sqrt{\gamma_{\mathrm{B},1}}\bar{S}^{\mathrm{N}}_{\mathrm{B}}(t) + \sqrt{\gamma_{\mathrm{R},1}}\bar{S}^{\mathrm{N}}_{\mathrm{R}}(t) \\
\dot{\bar{b}}(t) &= i(\Omega - \Omega_{\mathrm{B}})\bar{b}(t) - \frac{\Gamma}{2}\bar{b}(t) - ig^*\bar{a}_{\mathrm{p}}(t)\bar{a}^{\dagger}_{\mathrm{s}}(t) + \bar{\eta}(t) \\
\dot{\bar{a}}_{\mathrm{p}}(t) &= i(\omega_{\mathrm{p}} - \omega_2^m)\bar{a}_{\mathrm{p}}(t) - \frac{\gamma_{\mathrm{tot},2}}{2}\bar{a}_{\mathrm{p}}(t) - ig\bar{a}_{\mathrm{s}}(t)\bar{b}(t) + \sqrt{\gamma_{\mathrm{A},2}}\bar{S}^{\mathrm{in}}_{\mathrm{p}}(t) + \sqrt{\gamma_{\mathrm{tot},2}}\bar{S}^{\mathrm{N}}_{\mathrm{tot},2}(t),
\end{aligned} \tag{2}$$

where $a_{\mathrm{s}}(t) = \bar{a}_{\mathrm{s}}(t)\exp(-i\omega_{\mathrm{s}}t)$, $a_{\mathrm{p}}(t) = \bar{a}_{\mathrm{p}}(t)\exp(-i\omega_{\mathrm{p}}t)$, and $b(t) = \bar{b}(t)\exp(-i\Omega t)$); $\bar{\eta}(t)$, $\bar{S}^{\mathrm{in}}(t)$,$\bar{S}^{\mathrm{N}}_{(A,B,R)}(t)$, $\bar{S}^{\mathrm{N}}_{\mathrm{tot},2}(t)$, and $\bar{S}^{\mathrm{in}}_{\mathrm{p}}(t)$ are shifted in like manner. We also note that the above requires $\omega_{\mathrm{p}} = \omega_{\mathrm{s}} + \Omega$, consistent with our experimental scheme.

For simplicity, we treat the pump wave as undepleted (i.e., $\dot{\bar{a}}_{\mathrm{p}} = 0$ and $\bar{a}_{\mathrm{p}}(t) = \bar{a}_{\mathrm{p}}$) and ignore the vacuum fluctuations associated with the pump. We next take a Fourier transform of Eq. 2 in time, yielding

$$\begin{aligned}
-i\omega\bar{a}_{\mathrm{s}}[\omega] &= i(\omega_{\mathrm{s}} - \omega_1^n)\bar{a}_{\mathrm{s}}[\omega] - \frac{\gamma_{\mathrm{tot},1}}{2}\bar{a}_{\mathrm{s}}[\omega] - ig^*\bar{a}_{\mathrm{p}}\bar{b}^{\dagger}[\omega] + \sqrt{\gamma_{\mathrm{A},1}}\bar{S}^{\mathrm{in}}[\omega] + \sqrt{\gamma_{\mathrm{A},1}}\bar{S}^{\mathrm{N}}_{\mathrm{A}}[\omega] + \sqrt{\gamma_{\mathrm{B},1}}\bar{S}^{\mathrm{N}}_{\mathrm{B}}[\omega] + \sqrt{\gamma_{\mathrm{R},1}}\bar{S}^{\mathrm{N}}_{\mathrm{R}}[\omega] \\
-i\omega\bar{b}[\omega] &= i(\Omega - \Omega_{\mathrm{B}})\bar{b}[\omega] - \frac{\Gamma}{2}\bar{b}[\omega] - ig^*\bar{a}_{\mathrm{p}}\bar{a}^{\dagger}_{\mathrm{s}}[\omega] + \bar{\eta}[\omega].
\end{aligned} \tag{3}$$

Next, we solve these two coupled equations, yielding

$$\begin{aligned}
\bar{a}_{\mathrm{s}}[\omega_{\mathrm{s}},\omega] = \frac{1}{-i(\omega+\omega_{\mathrm{s}}-\omega_1^n) + \frac{\gamma_{\mathrm{tot},1}}{2} - \frac{|g|^2|\bar{a}_{\mathrm{p}}|^2}{i(\omega+\Omega-\Omega_{\mathrm{B}})+\frac{\Gamma}{2}}}\Bigg[&\sqrt{\gamma_{\mathrm{A},1}}\bar{S}^{\mathrm{in}}[\omega] \\
&+ \frac{-ig^*\bar{a}_{\mathrm{p}}\bar{\eta}^{\dagger}[\omega]}{i(\omega+\omega_{\mathrm{p}}-\omega_{\mathrm{s}}-\Omega_{\mathrm{B}})+\frac{\Gamma}{2}} + \sqrt{\gamma_{\mathrm{A},1}}\bar{S}^{\mathrm{N}}_{\mathrm{A}}[\omega] + \sqrt{\gamma_{\mathrm{B},1}}\bar{S}^{\mathrm{N}}_{\mathrm{B}}[\omega] + \sqrt{\gamma_{\mathrm{R},1}}\bar{S}^{\mathrm{N}}_{\mathrm{R}}[\omega]\Bigg].
\end{aligned} \tag{4}$$

We proceed by transforming out of the rotating frame and calculating the output signal spectrum by noting that $S^{\mathrm{out}}[\omega_{\mathrm{s}},\omega] = \sqrt{\gamma_{\mathrm{B},1}}a_{\mathrm{s}}[\omega_{\mathrm{s}},\omega] - S^{\mathrm{N}}_{\mathrm{B}}[\omega]$, yielding

$$S^{\mathrm{out}}[\omega_{\mathrm{s}},\omega] = T[\omega_{\mathrm{s}},\omega]\left[\sqrt{\gamma_{\mathrm{A},1}}S^{\mathrm{in}}[\omega_{\mathrm{s}}+\omega] + \frac{-ig^*\bar{a}_{\mathrm{p}}\bar{\eta}^{\dagger}[\omega]}{i(\omega+\Omega-\Omega_{\mathrm{B}})+\frac{\Gamma}{2}} + \sqrt{\gamma_{\mathrm{A},1}}\bar{S}^{\mathrm{N}}_{\mathrm{A}}[\omega] + \sqrt{\gamma_{\mathrm{B},1}}\bar{S}^{\mathrm{N}}_{\mathrm{B}}[\omega] + \sqrt{\gamma_{\mathrm{R},1}}\bar{S}^{\mathrm{N}}_{\mathrm{R}}[\omega]\right] - \bar{S}^{\mathrm{N}}_{\mathrm{B}}[\omega], \tag{5}$$

where we define the resonator transfer function ($T[\omega_{\mathrm{s}},\omega]$) as

$$T[\omega_{\mathrm{s}},\omega] \equiv \frac{\sqrt{\gamma_{\mathrm{B},1}}}{-i(\omega+\omega_{\mathrm{s}}-\omega_1^n) + \frac{\gamma_{\mathrm{tot},1}}{2} - \frac{|g|^2|\bar{a}_{\mathrm{p}}|^2}{i(\omega+\omega_{\mathrm{p}}-\omega_{\mathrm{s}}-\Omega_{\mathrm{B}})+\frac{\Gamma}{2}}}. \tag{6}$$

We proceed by computing the output power spectral density ($\mathfrak{S}^{\mathrm{out}}[\omega] = \lim_{T\to\infty}(1/T)|S^{\mathrm{out}}[\omega]|^2$, where T represents time [3]). This yields

$$\begin{aligned}
\mathfrak{S}^{\mathrm{out}}[\omega_{\mathrm{s}},\omega] = |T[\omega_{\mathrm{s}},\omega]|^2\Bigg[&\underbrace{\gamma_{\mathrm{A},1}\mathfrak{S}^{\mathrm{in}}[\omega_{\mathrm{s}}+\omega]}_{\text{Input Signal}} + \underbrace{\frac{G_{\mathrm{B}}Pv_{\mathrm{g},1}\Gamma^2(n_{\mathrm{th}}+1)}{4((\omega+\omega_{\mathrm{p}}-\omega_{\mathrm{s}}-\Omega_{\mathrm{B}})^2+(\frac{\Gamma}{2})^2)}}_{\text{Thermal}-\text{mechanical Noise}} \\
&\underbrace{+\gamma_{\mathrm{A},1}\mathfrak{S}^{\mathrm{N}}_{\mathrm{A}}[\omega_{\mathrm{s}}+\omega] + |\sqrt{\gamma_{\mathrm{B},1}} - \frac{1}{T[\omega_{\mathrm{s}},\omega]}|^2\mathfrak{S}^{\mathrm{N}}_{\mathrm{B}}[\omega_{\mathrm{s}}+\omega] + \gamma_{\mathrm{R},1}\mathfrak{S}^{\mathrm{N}}_{\mathrm{R}}[\omega_{\mathrm{s}}+\omega]}_{\text{Optical Vacuum Fluctuations}}\Bigg],
\end{aligned} \tag{7}$$

where $\mathfrak{S}^{\mathrm{in}}[\omega_{\mathrm{s}}+\omega]$ is the power spectral density of the input signal, $\mathfrak{S}^{\mathrm{N}}_{(\mathrm{A,B,R})}[\omega_{\mathrm{s}}+\omega]$ are the power spectral densities of the optical vacuum fluctuations, and the Brillouin gain coefficient G_{B} is defined as $G_{\mathrm{B}} = 4|g|^2|a_{\mathrm{p}}|^2/(P\Gamma v_{\mathrm{g},1})$ [4].

Equation 7 reveals three distinct terms in the output power spectrum; the first term gives the resonant amplification of the input signal, the second arises from thermal-mechanical noise, and the last results from optical vacuum fluctuations. We note here that the cross-terms vanish because the signal and noise sources are uncorrelated (e.g., $\eta^\dagger[\omega]S^{\rm in}[\omega_{\rm s}+\omega] \propto FT[\langle\eta^\dagger(t+\tau)S^{\rm in}(t)\rangle] = 0$).

We first calculate the signal-wave amplification ($|S^{\rm out}[\omega_{\rm s},0]|^2/|S^{\rm in}[\omega_{\rm s},0]|^2$) by analyzing the spectrum at the center frequency of the input signal (i.e., $\omega = 0$) and ignoring the noise terms, which yields

$$\frac{|S^{\rm out}[\omega_{\rm s},0]|^2}{|S^{\rm in}[\omega_{\rm s},0]|^2} = \left|\frac{\sqrt{\gamma_{\rm A,1}}\sqrt{\gamma_{\rm B,1}}}{-i(\omega_{\rm s}-\omega_1^n)+\frac{\gamma_{\rm tot,1}}{2}-\frac{G_{\rm B}Pv_{\rm g,1}\Gamma/4}{i(\omega_{\rm p}-\omega_{\rm s}-\Omega_{\rm B})+\Gamma/2}}\right|^2. \tag{8}$$

This is the central result of this section. We consider the effects of noise in the following section.

B. Noise dynamics

Building on this framework, we can also analyze the quantum-limited noise figure for the amplifier system. The noise figure is defined by

$$\mathrm{NF} = \frac{\mathrm{SNR}_1}{\mathrm{SNR}_2}, \tag{9}$$

where SNR_1 is the input signal-to-noise ratio (SNR) and SNR_2 is the output signal-to-noise ratio.

As an upper bound on the noise figure, we assume a quantum-limited input signal (i.e., signal relative to the zero-point background; for more details see Ref. [5, 6]). We consider the output SNR over a vanishingly small bandwidth $2\Delta\omega$ ($\Delta\omega \ll \Gamma$) centered around $\omega = 0$. The noise sources are given by the amplified thermal-mechanical and optical vacuum fluctuations (see Eq. 7), while the output signal is given by the amplified input signal. For simplicity, we assume the following functional form for the input signal spectrum: $\mathfrak{S}^{\rm in}[\omega_{\rm s}+\omega] = |S^{\rm in}|^2\delta(\omega)$, such that

$$\begin{aligned}\mathrm{SNR}_2 &= \frac{\int_{-\Delta\omega}^{\Delta\omega} d\omega\gamma_{\rm A,1}|S^{\rm in}|^2\delta(\omega)}{\int_{-\Delta\omega}^{\Delta\omega} d\omega\left[N_{\rm b}[\omega_{\rm s},\omega]+\gamma_{\rm A,1}\mathfrak{S}^{\rm N}_{\rm A}[\omega_{\rm s}+\omega]+|\sqrt{\gamma_{\rm B,1}}-\frac{1}{T[\omega_{\rm s},\omega]}|^2\mathfrak{S}^{\rm N}_{\rm B}[\omega_{\rm s}+\omega]+\gamma_{\rm R,1}\mathfrak{S}^{\rm N}_{\rm R}[\omega_{\rm s}+\omega]\right]} \\ &\simeq \frac{\gamma_{\rm A,1}|S^{\rm in}|^2}{2\Delta\omega\left[N_{\rm b}[\omega_{\rm s},0]+\left(\gamma_{\rm A,1}+|\sqrt{\gamma_{\rm B,1}}-\frac{1}{T[\omega_{\rm s},0]}|^2+\gamma_{\rm R,1}\right)\right]}\end{aligned} \tag{10}$$

where $N_{\rm b}[\omega_{\rm s},\omega]$ is defined by

$$N_{\rm b}[\omega_{\rm s},\omega] \equiv \frac{G_{\rm B}Pv_{\rm g,1}\Gamma^2(n_{\rm th}+1)}{4((\omega+\omega_{\rm p}-\omega_{\rm s}-\Omega_{\rm B})^2+(\frac{\Gamma}{2})^2)}. \tag{11}$$

Here, we have used the correlation properties of the optical vacuum fluctuations to compute each power spectral density (i.e., $\mathfrak{S}^{\rm N}_{\rm (A,B,R)}[\omega'] = \int_{-\infty}^{\infty} d\tau\langle S^{\rm N}_{\rm (A,B,R)}(t+\tau)S^{\rm N\dagger}_{\rm (A,B,R)}(t)\rangle e^{i\omega\tau} = \int_{-\infty}^{\infty} d\tau\delta(\tau)e^{i\omega'\tau} = 1)$).

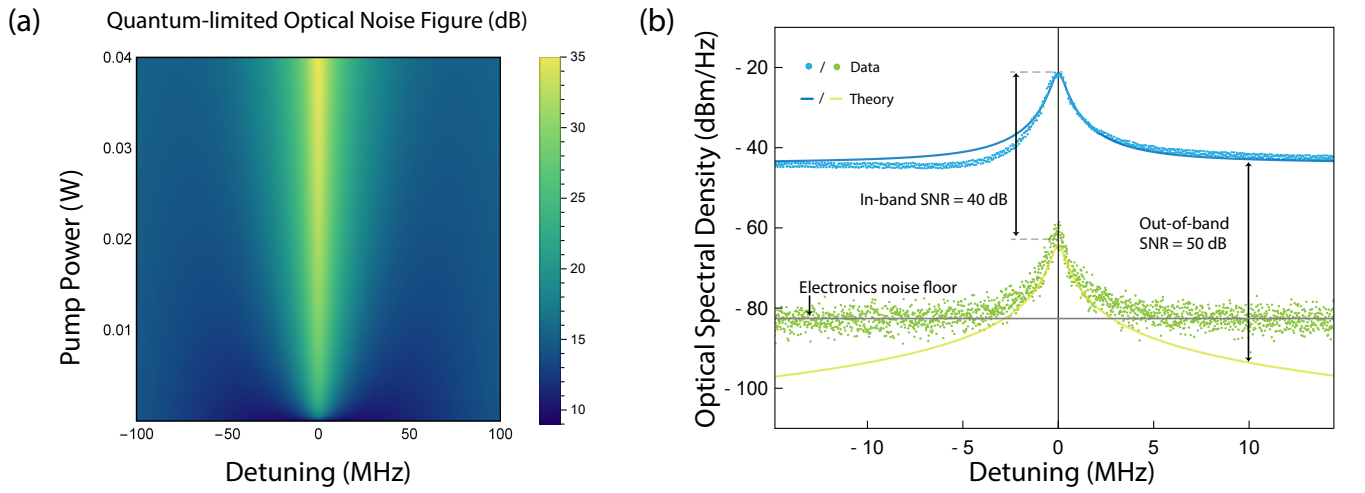

Fig. 1. (a) Theoretical quantum-limited optical noise figure (relative to quantum-limited input signal) as a function of detuning and pump power, obtained from Eq. 13. (b) Output signal (blue), Brillouin noise (light green), and respective theory curves (obtained from Eq. 7, with $P_p = 0.93P_{\rm th}$, where $P_{\rm th}$ is the laser threshold power). Data recorded with RBW = 50 KHz. Theory curves obtained from Eq. 7.

We next calculate the input SNR. To calculate an upper bound on the noise figure, we assume a quantum-limited input signal (i.e., limited only by optical vacuum fluctuations). In this case, the input SNR is given by

$$\begin{aligned} \mathrm{SNR}_1 &= \frac{\int_{-\Delta\omega}^{\Delta\omega} d\omega |S^{\mathrm{in}}|^2 \delta(\omega)}{\int_{-\Delta\omega}^{\Delta\omega} d\omega \mathfrak{S}_{\mathrm{A}}^{\mathrm{N}}[\omega]} \\ &= \frac{|S^{\mathrm{in}}|^2}{2\Delta\omega}. \end{aligned} \tag{12}$$

Now, combining Eq. 10 with Eq. 12, we calculate the noise figure of the system, yielding

$$\begin{aligned} \mathrm{NF} &= \frac{\left[N_{\mathrm{b}}[\omega_{\mathrm{s}},0] + \left(\gamma_{\mathrm{A},1} + |\sqrt{\gamma_{\mathrm{B},1}} - \frac{1}{T[\omega_{\mathrm{s}},0]}|^2 + \gamma_{\mathrm{R},1}\right)\right]}{\gamma_{\mathrm{A},1}} \\ &= \frac{\left[\frac{G_{\mathrm{B}} P v_{\mathrm{g},1} \Gamma^2 (n_{\mathrm{th}}+1)}{4((\omega_{\mathrm{p}}-\omega_{\mathrm{s}}-\Omega_{\mathrm{B}})^2+(\frac{\Gamma}{2})^2)} + \left(\gamma_{\mathrm{A},1} + |\sqrt{\gamma_{\mathrm{B},1}} - \frac{-i(\omega_{\mathrm{s}}-\omega_1^n)+\frac{\gamma_{\mathrm{tot},1}}{2} - \frac{|g|^2|a_{\mathrm{p}}|^2}{-i(\omega_{\mathrm{p}}-\omega_{\mathrm{s}}-\Omega_{\mathrm{B}})+\frac{\Gamma}{2}}}{\sqrt{\gamma_{\mathrm{B},1}}}|^2 + \gamma_{\mathrm{R},1}\right)\right]}{\gamma_{\mathrm{A},1}} \end{aligned} \tag{13}$$

We note that the noise figure is signal independent, as it should be [5]. Figure 1a plots the noise figure (Eq. 13) as a function of pump power and detuning from resonance. In the limit of low pump powers or large detunings, Eq. 13 converges to a value that is consistent with the loss produced by linear transmission through the system. When the pump power is increased, additional noise is imparted through spontaneous Brillouin scattering. As the pump power approaches the laser threshold, the quantum-limited noise figure of this silicon Brillouin amplifier system is approximately 36 dB relative to the zero-point background. This value is on par with the noise figure of conventional Brillouin amplifiers based on linear waveguides (which can range anywhere between 25 dB to 45 dB depending on the Brillouin frequency) [7]. In Brillouin amplifiers (such as the present system), the spontaneous Brillouin emission is narrowly centered around the Brillouin frequency (within ~ 10 MHz), and as such, this system exhibits low out-of-band noise; analyzing the performance of this system over larger bandwidths (~ 300 MHz), for example, yields an effective noise figure that is significantly reduced (NF ≈ 13 dB). Moreover, in many practical applications, the input signal typically possesses additional noise—such as relative intensity noise (RIN), amplified spontaneous emission (ASE), or relaxation oscillations—whose magnitude far exceeds the zero-point background [8]. Thus, while the quantum-limited noise figure we derive here provides a well-defined upper bound (worst case), the effective noise figure will be more favorable for a large range of practical applications.

B.1. Experimental measure of noise

We investigate the noise properties of this resonantly enhanced Brillouin amplifier through optical heterodyne laser spectroscopy using the apparatus diagrammed in Fig. 2a of the main text. Figure 1b plots the transmitted signal wave (blue) and the spontaneous optical spectrum (green) versus frequency detuning (relative to the Brillouin frequency Ω_{B}), demonstrating good agreement with theoretical predictions (see Eq. 7). These results highlight the low out-of-band noise properties of the Brillouin amplifier system.

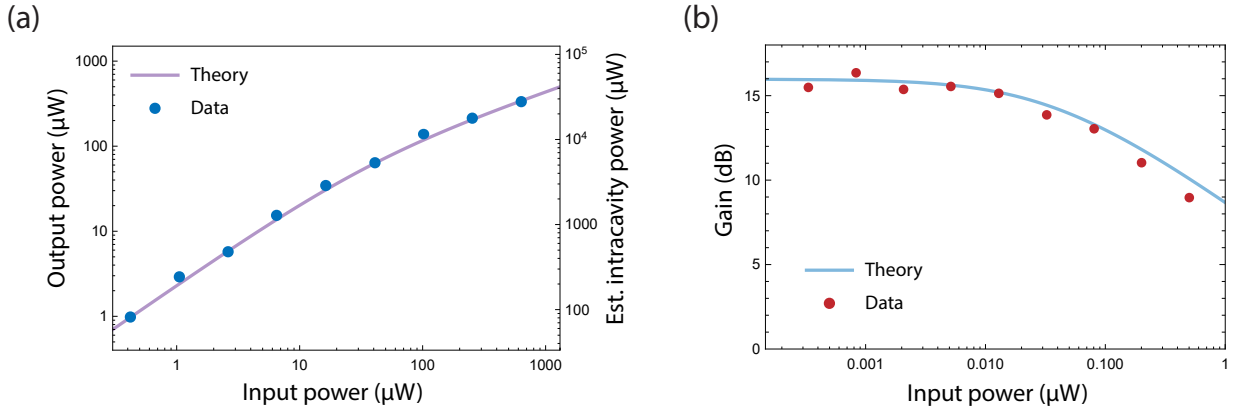

Fig. 2. (a) Output signal wave power as a function of input signal wave power. (b) Gain versus input power. Theoretical curves are obtained by numerically solving Eq. 15 (with $P = 0.86P_{\mathrm{th}}$, $\mu_{\mathrm{A},1}^2 = 0.16$, and $\mu_{\mathrm{B},1}^2 = 0.012$).

C. Gain depletion

In this section, we explore the output signal saturation that arises from pump depletion within the resonator. We begin with the mean-field equations of motion under the rotating-wave approximation (Eq. 2). Here, we no longer assume a stiff pump; instead, we adiabatically eliminate the pump dynamics, in accodance with the separation of time scales ($\gamma_{\mathrm{p}} \gg \gamma_{\mathrm{s}} \gg \Gamma$).

In this case, the slowly varying amplitude of the pump wave is given by

$$\bar{a}_{\mathrm{p}}(t) = \frac{2}{\gamma_{\mathrm{tot},2}}\left[-ig\bar{a}_{\mathrm{s}}(t)\bar{b}(t) + \sqrt{\gamma_{\mathrm{A},2}}\bar{S}_{\mathrm{p}}^{\mathrm{in}}(t)\right]. \tag{14}$$

Next, we substitute Eq. 14 into Eq. 2, ignore thermal and quantum fluctuations, and solve for the steady-state behavior of the system, yielding the following transcendental equation for the signal wave field:

$$\bar{a}_{\mathrm{s}} = \frac{\sqrt{\gamma_{\mathrm{A},1}}\bar{S}_{\mathrm{s}}^{\mathrm{in}}}{\left[-i(\omega_{\mathrm{s}}-\omega_1^n) + \frac{\gamma_{\mathrm{tot},1}}{2} + \frac{G_{\mathrm{B}}^2\hbar\omega_{\mathrm{p}}Pv_{\mathrm{g},1}^2v_{\mathrm{g},2}\Gamma^2/(8\gamma_{\mathrm{tot},2}L)}{(\omega_{\mathrm{p}}-\omega_{\mathrm{s}}-\Omega_{\mathrm{B}})^2+(\Gamma/2+G_{\mathrm{B}}\hbar\omega_{\mathrm{p}}v_{\mathrm{g},1}v_{\mathrm{g},2}\Gamma|\bar{a}_{\mathrm{s}}|^2/(2\gamma_{\mathrm{tot},2}L))^2} - \frac{G_{\mathrm{B}}Pv_{\mathrm{g},1}\Gamma/4}{i(\omega_{\mathrm{p}}-\omega_{\mathrm{s}}-\Omega_{\mathrm{B}})+\Gamma/2+G_{\mathrm{B}}\hbar\omega_{\mathrm{p}}v_{\mathrm{g},1}v_{\mathrm{g},2}\Gamma|\bar{a}_{\mathrm{s}}|^2/(2\gamma_{\mathrm{tot},2}L)}\right]}. \tag{15}$$

As this equation becomes analytically intractable, we proceed by solving Eq. 15 numerically.

We also explore this gain depletion behavior through a set of systematic experimental studies. This approach involves analyzing the transmitted signal-wave spectrum versus frequency over a range of input signal-wave powers; data from these measurements are presented in Fig. 2. Through these measurements, we observe a clear reduction in the gain as we increase the input signal wave power, in good agreement with our pump-depletion-based theoretical predictions.

2. PASSIVE DEVICE PROPERTIES

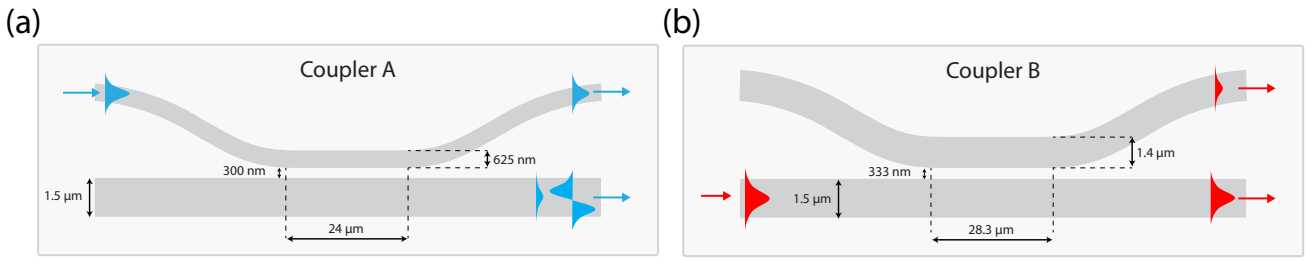

Fig. 3. (a) Diagram illustrating the design of coupler A. (b) Diagram and dimensions of coupler B.

A. Multimode and mode-specific couplers

Here we explain the design of the multimode and mode-specific couplers (i.e., couplers A and B, respectively) used in the resonantly enhanced Brillouin amplifier.

Coupler A is a directional coupler that is designed to produce non-zero overlap with both spatial modes of the racetrack waveguide. As shown in Fig. 3a, it consists of a 625-nm bus waveguide whose fundamental (symmetric) mode is primarily phase-matched with the antisymmetric spatial mode of the 1.5-μm racetrack waveguide, such that it couples strongly to the antisymmetric spatial mode and weakly to the symmetric spatial mode (see Table 1).

Coupler B is an asymmetric multimode directional coupler that is designed to couple primarily to the symmetric spatial mode of the racetrack waveguide. As shown in Fig. 3b, the widths of the bus and racetrack waveguides are slightly asymmetric (1.4 μm and 1.5 μm, respectively), such that the fundamental modes remain phase-matched (the fundamental mode indices remain very close), while the higher order modes are not phase-matched (the mode indices become quite distinct), yielding a coupler that selectively couples out the symmetric mode (with crosstalk of $\sim$ 10 dB; see Table 1 for more details). In practice, this leads to a small degree of pump light (as low as $\sim$ 200 μW) exiting coupler B. For future systems demonstrations, the residual pump light could readily be suppressed by improving the mode selectivity of the coupler or by using some combination of wavelength-selective filtering [9] and interference cancellation [10] to drive the pump levels down by an additional 60-80 dB.

B. Resonator properties

In this section, we present a brief explanation of the passive resonator properties. The multi-spatial-mode racetrack cavity produces two distinct sets of cavity modes, yielding a characteristic multimode transmission spectrum (see Fig. 4c). We measure the linear transmission response of the cavity using a swept 1.55 μm laser (Agilent 81600B; sweep rate set to 5 nm/s) at low powers ($\sim$ 120 μW on-chip). Fig. 4a-b plots the measured transmission (thru) spectra centered around two distinct mode pairs that satisfy the Brillouin condition ($\omega_1^n = \omega_2^m - \Omega_{\mathrm{B}}$), while Fig. 4c shows the transmission spectra measured at the thru and drop ports over a larger wavelength range. Fitting these transmission spectra to a multimode resonator model (see Supplmentary Materials of Ref. [1]) allows us to obtain important parameters of the system, including the multimode coupling coefficients, group velocities, and linear propagation losses (see Table 1). This information is then used to model the amplifier dynamics (for example, see theory curve in Fig. 2d-e of the main text).

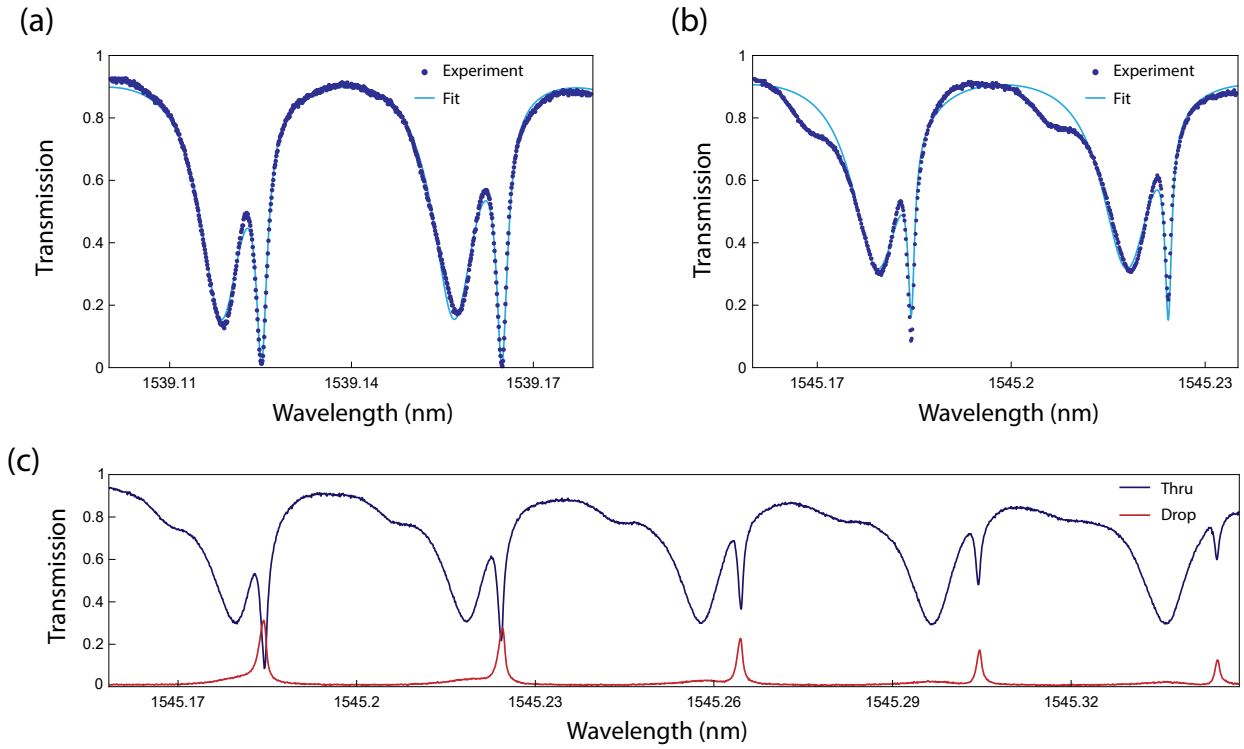

Fig. 4. (a)-(b) Linear (thru) transmission spectra centered around two distinct mode pairs that satisfy the Brillouin condition ($\omega_1^n = \omega_2^m - \Omega_B$). Narrow (broad) resonances correspond to the symmetric (antisymmetric) spatial modes of the multimode waveguide. Fits are obtained using the multimode ring resonantor theory presented in the Supplementary Materials of Ref. [1]. (c) Transmission spectra measured at the thru and drop ports over a larger wavelength range.

3. EXPERIMENTAL CONSIDERATIONS AND DATA ANALYSIS

A. Nonreciprocal amplification characterization

An important feature of this Brillouin system is that the amplificaiton process is inherently nonreciprocal. This property arises from the time modulation induced and sustained by the coherent phonon field. Alternatively, this phenomena can also be understood through the energy and phase-matching conditions required by this traveling-wave process (see Fig. 5b-c). The phonon field that mediates the Brillouin amplification cannot mediate coupling in the backward direction as a result of phase-matching. Moreover, the phonon frequency and wavevector that would be required for a backward process (between counter-propagating waves) is not supported by the acoustic dispersion relation. These phase-matching and energy-conservation considerations are illustrated succinctly by the diagrams presented in Fig. 5b-c.

We next detail the experimental approach and apparatus used to investigate the nonreciprocal nature of this resonantly enhanced Brillouin amplifier (data presented in Fig. 3c of the main text). As diagrammed in Fig. 5a, these measurements involve the use of a fiber-optic switch, which allows us to rapidly change the propagation direction of the signal wave relative to the pump wave. Throughout the experiments, the pump wave is coupled into a counter-clockwise antisymmetric mode of the resonator that is separated from a symmetric cavity mode by the Brillouin frequency ($\omega_p = \omega_2^m, \omega_2^m - \omega_1^n = \Omega_B$). We then measure the signal wave transmission in the forward and backward directions as we sweep the signal-wave frequency $\omega_s = \omega_p - \Omega$ through the dual resonance condition ($\omega_s = \omega_1^n = \omega_p - \Omega_B$).

B. System parameters and data analysis

In this section, we detail the experimental parameters of the system and how they are determined. All parameters in the system are corroborated by a self-consistent model of the amplifier dynamics. We enumerate these parameters in Table 1. The passive optical properties of the resonator system are obtained by fitting the transmission spectrum to a multi-spatial-mode resonator model (for more details, see section 3 of this supplement and Supplementary Materials of Ref. [1]). As the couplers A and B are wavelength dependent, we indicate an approximate range for each coupling coefficient. The acoustic dissipation rate is determined by analyzing the Brillouin-gain bandwidths at low intracavity pump powers. The Brillouin-gain coefficient is extracted by fitting the mean-field model to our measurements (see Fig. 2c of the main text). Altogether, these parameters are in agreement with those previously obtained in similar device geometries [1].

To determine the degree of net amplification (for Fig. 2 of the main text), we calibrate the signal-wave transmission through the resonant system by comparing it to the signal-wave transmission through a linear device on the same chip (placed 600 μm away). Data for Fig. 2c-d of the main text were obtained by acquiring traces as the signal-wave detuning (Ω) is swept through the Brillouin

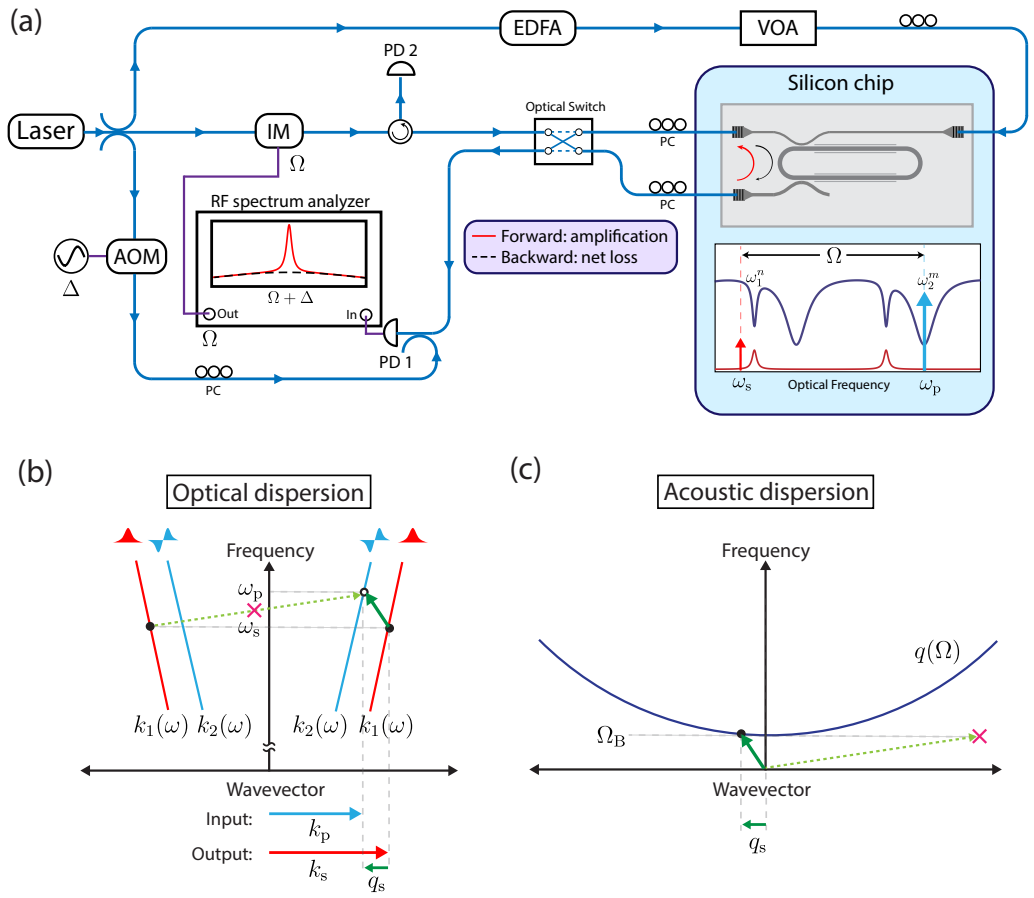

Fig. 5. Nonreciprocal optical amplification measurements. (a) Diagram of the experimental apparatus used to characterize the nonreciprocal nature of the resonantly enhanced Brillouin amplifier. Laser light is split along three paths. The first (top) is used to generate a pump wave of a desired optical power, which is subsequently coupled on-chip. The second arm synthesizes the signal wave with the desired frequency detuning ($\Omega = \omega_\mathrm{p} - \omega_\mathrm{s}$) using an intensity modulator (IM). Finally, the third creates an optical local oscillator (LO) using an acousto-optic modulator (AOM), which blueshifts the light by $\Delta = 44$ MHz. An optical switch directs the signal wave light on-chip such that it either co- or counter-propagates with the pump wave within the resonator. After passing through the device, the signal wave is coupled through the drop port and off-chip, where it is combined with the blueshifted LO and measured on a high-speed photodector (PD 1). (b)-(c) diagrams illustrating energy and phase-matching conditions imposed by the optical and acoustic dispersion relations. In this diagram, the dark green arrow represents the frequency and wavevector of the phonon that mediates stimulated intermodal Brillouin scattering, while the dotted light-green arrow shows the phonon that would be required to mediate amplification in the backward direction, which is not supported by the acoustic dispersion relation. Thus, the elastic wave that mediates forward stimulated intermodal Brillouin scattering does not mediate a backward scattering process.

frequency (Ω_B)) while sweeping the the pump power and varying pump wavelength around the dual-resonance condition (i.e., $\omega_\mathrm{p} = \omega_2^m$, $\omega_\mathrm{p} - \Omega_\mathrm{B} = \omega_1^n$). The data in Fig. 2c-d represent the traces obtained with near-zero detuning ($\omega_\mathrm{p} - \Omega_\mathrm{B} - \omega_1^n$). Intracavity powers are estimated using the passive ring resonator parameters and accounting for the effects of nonlinear loss (studied in detail in the supplementary information of Ref. [11]); additionally, this analysis is consistent with the power-dependent nature of the directional couplers.

C. Device fabrication

The Brillouin amplifier devices are fabricated on a single-crystal silicon-on-insulator chip (215 nm silicon, 3 μm SiO_2) using a two-step electron-beam lithography process (for additional details, see [1, 11–13]). Optical waveguides are defined through electron-beam lithography (using hydrogen silsesquioxane (HSQ) electron-beam resist), followed by development in MF-312 and an anisotropic Cl_2 reactive ion etch (RIE), which removes 80 nm of silicon. A subsequent lithography step is used to pattern slots with CSAR electron-beam resist. After development in Xylenes, the remainder of the silicon is removed through another RIE etch, exposing the oxide underneath the slotted regions. Finally, a wet-etch (49% hydrofluoric acid) is used to remove the oxide undercladding to create a continuously suspended Brillouin-active waveguide. The phonon membrane dimensions are 2.85 μm × 135 nm, while the multimode optical ridge waveguide is 1.5 μm × 215 nm [1, 11].

Optical properties	Description	Value
L	Length of device	1.57 cm
W_{m}	Acoustic membrane width	2.85 μm
W_{o}	Optical waveguide width	1.5 μm
FSR_1	Free spectral range of symmetric mode	5.02 GHz
FSR_2	Free spectral range of antisymmetric mode	4.87 GHz
$\mu^2_{\mathrm{A},1}$	Coupling through coupler A into the symmetric mode	0.045-0.16
$\mu^2_{\mathrm{A},2}$	Coupling through coupler A into the antisymmetric mode	0.62-0.71
$\mu^2_{\mathrm{B},1}$	Coupling through coupler B into the symmetric mode	0.01-0.07
$\mu^2_{\mathrm{B},2}$	Coupling through coupler B into the antisymmetric mode	0.007-0.016
α_1	Symmetric spatial mode propagation loss	6.7 m^{-1}
α_2	Antisymmetric spatial mode propagation loss	20.6 m^{-1}
$v_{\mathrm{g},1}$	Symmetric spatial mode group velocity	7.91 $\times 10^7$ m/s
$v_{\mathrm{g},2}$	Antisymmetric spatial mode group velocity	7.67 $\times 10^7$ m/s
Ω_{B}	Brillouin frequency	2π 5.95 GHz
Γ	Acoustic dissipation rate	2π 9 MHz
G_{B}	Brillouin gain coefficient	380 $\mathrm{W}^{-1}\mathrm{m}^{-1}$

Table 1. Experimental parameters of the nonreciprocal resonantly enhanced silicon Brillouin amplifier.

REFERENCES

1. N. T. Otterstrom, R. O. Behunin, E. A. Kittlaus, Z. Wang, and P. T. Rakich, "A silicon Brillouin laser," Science **360**, 1113–1116 (2018).
2. B. E. Little, S. T. Chu, H. A. Haus, J. Foresi, and J.-P. Laine, "Microring resonator channel dropping filters," J. Light. Technol. **15**, 998–1005 (1997).
3. H. A. Haus, *Waves and fields in optoelectronics* (Prentice-Hall, 1984).
4. P. Kharel, R. Behunin, W. Renninger, and P. Rakich, "Noise and dynamics in forward Brillouin interactions," Phys. Rev. A **93**, 063806 (2016).
5. H. Haus, "The noise figure of optical amplifiers," IEEE Photonic Tech L **10**, 1602–1604 (1998).
6. B. Bristiel, S. Jiang, P. Gallion, and E. Pincemin, "New model of noise figure and rin transfer in fiber Raman amplifiers," IEEE Photonic Tech L. **18**, 980–982 (2006).
7. E. Desurvire, D. Bayart, B. Desthieux, and S. Bigo, *Erbium-doped fiber amplifiers: Device and System Developments*, vol. 2 (Wiley-Interscience New York, NY, 2002).
8. V. J. Urick, K. J. Williams, and J. D. McKinney, *Fundamentals of microwave photonics*, vol. 1 (John Wiley & Sons, 2015).
9. P. Dong, N.-N. Feng, D. Feng, W. Qian, H. Liang, D. C. Lee, B. Luff, T. Banwell, A. Agarwal, P. Toliver *et al.*, "GHz-bandwidth optical filters based on high-order silicon ring resonators," Opt. Express **18**, 23784–23789 (2010).
10. S. Liu, H. Cai, C. DeRose, P. Davids, A. Pomerene, A. Starbuck, D. Trotter, R. Camacho, J. Urayama, and A. Lentine, "High speed ultra-broadband amplitude modulators with ultrahigh extinction > 65 dB," Opt. Express **25**, 11254–11264 (2017).
11. E. A. Kittlaus, N. T. Otterstrom, and P. T. Rakich, "On-chip inter-modal Brillouin scattering," Nat. Commun. **8**, 15819 (2017).
12. E. A. Kittlaus, H. Shin, and P. T. Rakich, "Large Brillouin amplification in silicon," Nat. Photonics **10**, 463 (2016).
13. N. T. Otterstrom, R. O. Behunin, E. A. Kittlaus, and P. T. Rakich, "Optomechanical cooling in a continuous system," Phys. Rev. X **8**, 041034 (2018).